Electrochemical Detection of Viral Nucleic Acids by DNA Nanolock-Based Porous Electrode Device

Zhongnan Huang,[#] Wenjie Wang,[#] Yingfei Wang, Han Wang, Yimin Pang, Quan Yuan,* Jie Tan,* and Weihong Tan*

Cite This: *Anal. Chem.* 2023, 95, 16668−16676

Read Online

ACCESS | Metrics & More | Article Recommendations | Supporting Information

ABSTRACT: Developing rapid, sensitive, and facile nucleic acid detection technologies is of paramount importance for preventing and controlling infectious diseases. Benefiting from the advantages such as rapid response, low cost, and simple operation, electrochemical impedance spectroscopy holds great promise for point-of-care nucleic acid detection. However, the sensitivity of electrochemical impedance spectroscopy for low molecular weight nucleic acids testing is still limited. This work presents a DNA nanolock-based porous electrode to improve the sensitivity of electrochemical impedance spectroscopy. Once the target nucleic acids are recognized by the DNA probes, the pore-attached DNA nanolock caused remarkable impedance amplification by blocking the nanopores. Taking SARS-CoV-2 nucleic acid as a model analyte, the detection limit of the porous electrode was as low as 0.03 fM for both SARS-CoV-2 RNA and DNA. The integration of a porous electrode with a wireless communicating unit generates a portable detection

device that could be applied to direct SARS-CoV-2 nucleic acid testing in saliva samples. The portable device could effectively distinguish the COVID-19 positive and negative samples, showing a sensitivity of 100% and a specificity of 93%. Owing to its rapid, ultrasensitive, specific, and portable features, the as-designed DNA nanolock and porous electrode-based portable device holds great promise as a point-of-care platform for real-time screening of COVID-19 and other epidemics.
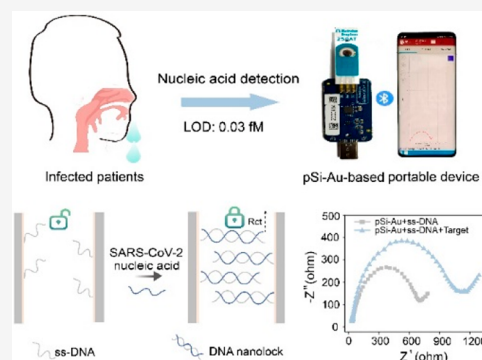
INTRODUCTION

Emerging infectious diseases have remained an important global problem in public health.[1−3] Establishing a method for rapid diagnosis of infectious disease and isolation of infected individuals can prevent further viral spread and are essential for controlling disease transmission.[4−7] At present, the reverse transcription quantitative polymerase chain reaction (RT-qPCR) has been regarded as a gold standard for infectious disease diagnoses. However, its lengthy processing time and requirement of specialized laboratories make it ill-suited for point-of-care tests.[8−10] A method that is suitable for point-of-care testing and able to detect infectious disease nucleic acid sensitively and rapidly is thus urgently required.[11,12]

Electrochemical biosensing technologies have attracted extensive research interest because of their low cost, rapid response, and portability.[8,13−15] These merits make the electrochemical biosensor a good candidate for point-of-care infectious disease diagnosis.[16] Electrochemical impedance spectroscopy can measure target concentrations via changes in the degree of crowding on electrode interface, avoiding tedious steps for addition and preservation of labeled probes, making detection operations and device integration much more accessible for further bedside diagnosis of infectious diseases.[17,18] However, in planar electrodes, due to the low molecular weight of nucleic acids, there is little change in the

degree of crowding before and after nucleic acid hybridization, resulting in an unobvious change in impedance, limiting the utility of electrochemical impedance spectroscopy for infectious disease nucleic acid testing.[19,20] A growing body of evidence suggests that the rigidity of nucleic acids can be enhanced greatly by forming a double-stranded complex, and their molecular volume would change more by confined structures of electrode interface.[21−23] Inspired by this, the nanopore structure with a high surface area was introduced into the electrodes.[24] Nucleic acids can block the pore by forming a rigid double-stranded structure, and this structure sharply reduces the real surface area of nanopore electrodes, thus amplifying changes of impedance value and addressing the sensitivity limitations of impedance methods toward detecting small nucleic acid molecules.[25−28]
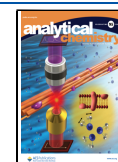
Here, by taking SARS-CoV-2 as a model analyte, we report an electrochemical impedance sensor based on a DNA nanolock to achieve nucleic acid detection with high

sensitivity. The results demonstrate that in the porous electrode with suitable pore sizes, the target nucleic acid can block the pore by binding to their complementary sequences. This DNA nanolock greatly amplifies the impedance responses and improves the detection sensitivity, achieving a limit of detection (LOD) of 0.03 fM for both SARS-CoV-2 RNA and DNA. It is also indicated that the spatial confinement effect in a porous electrode can effectively limit the reorganization of nucleic acids on the electrode surface and further improve the stability and reproducibility of the impedance signal. Finally, we validated our impedance sensor on 45 saliva samples, identifying 15 positive SARS-CoV-2 samples and 30 negative SARS-CoV-2 samples with a sample-to-answer time of 30 min. Sensitivity and specificity values of 100% and 93%, respectively, were calculated for saliva samples. Overall, the as-developed electrochemical impedance-based sensor with an attached DNA nanolock provides an effective means for efficient and real-time SARS-CoV-2 detection. Future work can be directed toward designing a miniaturized and integrated sensor capable of providing point-of-care detection on various nucleic acids of interest.

■ MATERIALS AND METHODS

Reagents and Materials. Si wafers (P++, 0.1 mΩ cm) were acquired from Siltronix co., Ltd. (France). Tetrachloroauric acid tetrahydrate ($HAuCl_4 \cdot 4H_2O$), hydrofluoric acid (HF, CAUTION: strong corrosive liquid), potassium ferricyanide ($K_3[Fe(CN)_6]$), potassium ferrocyanide ($K_4[Fe(CN)_6]$), potassium chloride (KCl), mercaptoethanol (MCH), and ethylene diamine tetraacetic acid (EDTA) were obtained from Aladdin Reagent Company (Shanghai, China). Concentrated sulfuric acid (H_2SO_4), potassium nitrate (KNO_3), ethanol, and hydrogen peroxide (H_2O_2) were bought from Sinopharm Chemical Reagent Co. Ltd. (Shanghai, China). All oligonucleotide sequences used in this study were synthesized by Hippobio (Huzhou, China). All other reagents were of analytical grade and used as received without further purification. Deionized (DI) water (resistivity ≈ 18.2 MΩ·cm) was used throughout the experiments.

Preparation of Porous Silicon Electrode (pSi). Briefly, pSi was prepared by the electrochemical etching of Si wafers in a two-electrode configuration using a platinum mesh counter electrode.[29] The Si wafers were contacted on the back side with a strip of aluminum foil and placed in a Teflon support. An O-ring with an exposed area of 0.785 cm² is placed on the front side of the Si wafer, and the etching area was defined by the O-ring. Then a Teflon cell cap containing a groove fitted with the size of the O-ring was tightly fixed to the Teflon support via four screws. The counter electrode was a platinum wire ring placed above the Si wafer. Prior to electrochemical etching, the Si wafers were sonicated in acetone and rinsed with ultrapure water. Electrochemical etching was performed at a constant current in electrolyte mixture solution of HF (49%) and ethanol (3:1, v/v).[30] After etching, the wafers were thoroughly rinsed with 95% ethanol and carefully dried in a N_2 flow for further characterization and applications.

Preparation of Gold Film-Modified Porous Electrode (pSi-Au) with Different Pore Sizes. A layer of gold film was electrochemically deposited on the pSi with different sizes in the same electrolysis vessel. The pSi and platinum meshes acted as the cathode and anode, respectively. The electrolysis vessel was filled with a solution of 0.001% $HAuCl_4$, and electrodeposition was conducted at a constant current of 5 mA

for 10 min. The resulting pSi-Au was rinsed with distilled water and ethanol for further use. For the assays of pore diameter regulation, the etching current was performed for 60 s at 0.045, 0.06, and 0.12 A, respectively, corresponding to 5 nm pSi-Au, 10 nm pSi-Au, and 40 nm pSi-Au, respectively. For the optimal experiments of pore depth, the etching current was performed constantly at 0.06 A, and the etching time was 300, 150, 60, 30, 15, and 6 s, respectively; the pore depths of pSi-Au were 10 μm, 5 μm, 2 μm, 1 μm, 0.5 μm, and 0.2 μm. The entire structure of pSi-Au was probed by the optical reflectivity. The gold film-modified flat electrode (fSi-Au) was obtained by directly depositing Au film on a Si wafer with the same electrode surface area.

Reflectance Spectra of pSi-Au Interface. A halogen tungsten lamp was used to illuminate the surface of pSi-Au through one arm of a bifurcated fiber optic cable at normal incidence with a focused spot area of 2 mm². The reflected light covering the wavelength range of 400−1000 nm was transmitted through another arm of the bifurcated fiber and was collected by the Spectra-Suite software (Ocean Optics). The effective optical thickness (EOT) was obtained from the as-followed Fabry-Pérot relationship[31]

$$2nL = m\lambda \tag{1}$$

where m is the spectral order and λ is the wavelength of light; n is the average refractive index of the porous layer, and L is the thickness of the porous layer. The value of the EOT was determined by the Fourier transformation of the reflectivity spectrum. Fourier transformation was calculated with the IGOR program (Wavemetrics, Inc.) and the calculated results produced an obvious peak whose position was equal to the product value of 2 nL in eq 1. The method described herein for detecting optical thickness is actually Fourier-transform reflectometric interference spectroscopy (FT-RIFS).

Fabrication of Porous Electrode Sensor. The porous electrode sensor was fabricated as follows. First, the single-stranded DNA oligonucleotides (ss-DNA) were dissolved in 50 mM Tris (hydroxymethyl) aminomethane-hydrochloric acid-ethylene diamine tetraacetic acid (Tris-HCl-EDTA) buffer (pH 7.4) to prepare the 1 μM thiolated sensing probe. The thiolated sensing probe was immobilized on the porous electrode surface through a Au-thiol bond after staying at 4 °C for 3 h, and then the free ss-DNA was removed by vigorously washing the electrode in distilled water. After drying for several minutes in air, the resulting electrode was designated as an ss-DNA-modified porous electrode for characterizations and applications. To achieve the electrochemical detection of target SARS-CoV-2 RNA, the 150 μL of target RNA with different concentrations (from 10^{-11} M to 10^{-15} M amounts) was immobilized on each ss-DNA-modified porous electrode by incubating at 4 °C for 30 min. Subsequently, the unreacted target RNA was washed away with distilled water. The impedance spectrum was investigated by EIS to estimate the sensing property for target SARS-CoV-2 RNA detection. To investigate whether the ss-DNA could hybridize to the target on a porous electrode, the optical thickness detection of porous electrode sensors was conducted by following the above-mentioned protocols. To investigate the selectivity of the porous electrode sensors, other interfering samples were tested under a similar procedure after replacing the target RNA with structurally similar nucleic acids.

Blinded Testing of Pseudovirus Samples. Saliva samples were kindly provided by healthy volunteers. Before
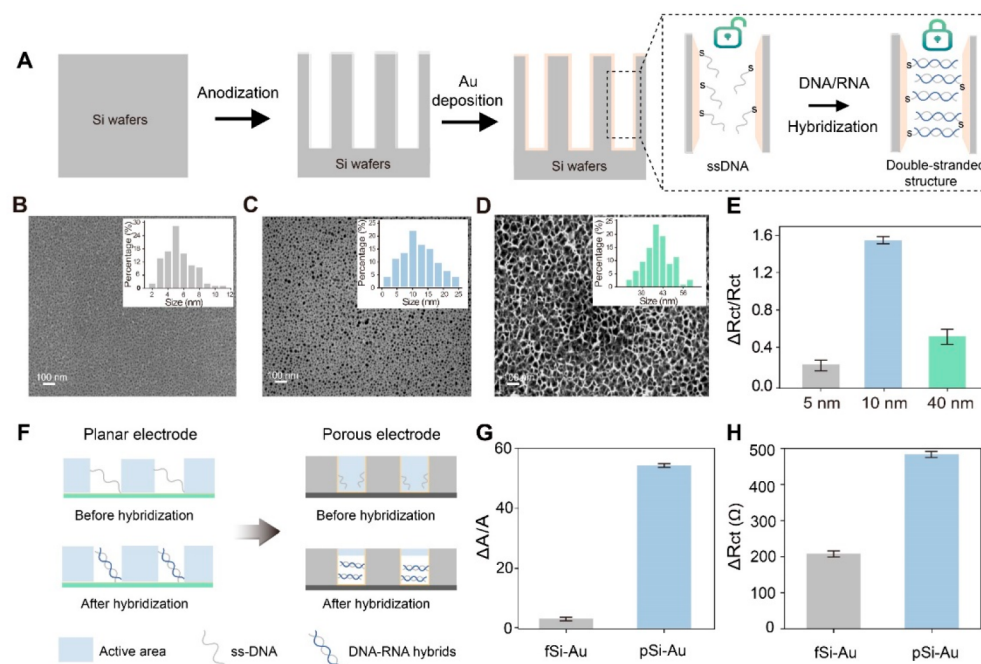
Figure 1. The fabrication and characterization of porous electrode for the detection of SARS-CoV-2 nucleic acid. (A) Schematic illustrating the fabrication process of the porous DNA nanolock electrode. (B–D) Scanning electron microscopy (SEM) images of porous electrode with pore sizes of 5 nm (B), 10 nm (C), and 40 nm (D), respectively. Inset: pore size distribution of porous electrode derived from panels B–D. (E) Impedance-based detection of SARS-CoV-2 RNA using porous electrode with different pore sizes; target RNA concentration: 10 pM. (F) Schematic of the change of electrode active area for the SARS-CoV-2 RNA identification using planar electrode (left) and porous electrode (right), respectively. The blue area represents the range of effective electrode area. (G) Changes in the electro-active surface area of the planar (gray) and porous electrodes (blue) before and after SARS-CoV-2 RNA was recognized. (H) The impedance changes of planar (gray) and porous electrodes (blue) after the SARS-CoV-2 RNA was identified. Error bars in panels E, G, and H are standard error measurements with $n = 3$.

collection, the subject was asked to gargle with 20 mL of saline for 1 min, and then the sterilized Eppendorf tube was placed on the oral mucosa of the subject's lower lip to allow saliva to flow in naturally, and 3 mL of nonirritating saliva sample was obtained. The obtained saliva samples were first centrifuged for 10 min (10000 rpm) at 4 °C and then diluted 10-fold with 0.1 M PBS (pH 6.0). Pseudovirus samples were prepared using SARS-CoV RNA spiked into saliva samples. The saliva samples delivered to the study team were split into three groups: interference group, control group, and positive group. The study team was blinded to the order and number of these samples. To establish the threshold shown, three samples of the patients with COVID-19 negative were used. The receiver operating characteristic (ROC) analysis was only made after revealing the study results to the polymerase chain reaction (PCR) team, who performed RT-qPCR determinations independently.

RESULTS AND DISCUSSION

Preparation and Characterization of DNA Nanolock-Based Porous Electrode. As shown in Figure 1A, the porous silicon electrode (pSi) was prepared by electrochemical etching of silicon, and a layer of gold film was further anodically deposited on the obtained pSi wafer (Au-pSi) (Figure S1). Thiol-modified single-stranded DNA oligonucleotide (ss-DNA) was attached to the gold-plated porous electrodes, and the ss-DNA assembles into double-stranded structure on addition of a complementary SARS-CoV-2 RNA gene target. Electrochemical impedance spectroscopy (EIS) was carried out to characterize the modification and hybridization of ss-DNA on a porous electrode (Figure S2).

Compared with the gold-plated porous electrode, the impedance of the ss-DNA-modified porous electrode was increased, indicating that the ss-DNA was successfully bound to the nanopores through Au-thiol bonding. After adding the target RNA sequence of SARS-CoV-2, the impedance of the ss-DNA-modified porous electrode was further increased, supporting that the complementary double-stranded structure was formed. These results indicate that we have successfully constructed a porous electrode that can bind to the SARS-CoV-2 RNA gene target.

The SARS-CoV-2 N gene encodes the most stable and conserved nucleocapsid (N) protein in the virus, and detection of it will allow for a more accurate diagnosis of SARS-CoV-2 infection.[32,33] Therefore, we chose the 20 bp SARS-CoV-2 N gene fragment as the target for the ss-DNA-functionalized porous electrodes (Table S1). Since the length of a single base is 0.34 nm, the theoretical length of the double-stranded nucleic acid structure formed by the ss-DNA and the target N gene is about 10 nm.[34−36] To investigate whether a remarkable impedance change requires the size matching between pore size and theoretical length of the double-stranded nucleic acid structure, we constructed nucleic acid double-stranded structures on porous electrodes with pore sizes of 5, 10, and 40 nm. Then, we characterized the impedance changes of porous electrodes before and after formation of nucleic acid double-stranded structure using EIS (Figure 1B–D). It is reported that the increased degree of the impedance is related to the pore size.[37] This was probably due to the pore size matching the theoretical length of nucleic acid double-stranded structures. In comparison with the porous electrodes with pore sizes centered at 5 and 40 nm, the porous electrode that has an

average pore size of 10 nm showed the greatest increase in impedance responses (Figure 1E). This result is consistent with the theoretical predictions of pore size. In addition, to determine the best conditions for the detection of the N gene, several conditions of pore depth, ss-DNA concentration, and incubation time with target were evaluated. The impedance changes of the porous electrode gradually increased and stabilized with increasing pore depth, ss-DNA concentration, and extended incubation time. Under the optimized conditions of pore depth (2 μm), ss-DNA concentration (100 nM), and incubation time (30 min), the impedance change of the porous electrode eventually plateaued (Figure S3). Therefore, we chose a pore size of 10 nm, a pore depth of 2 μm, an ss-DNA concentration of 100 nM, and an incubation time of 30 min for the detection of the SARS-CoV-2 N gene.

It is well-known that the change in the electrochemical active area is a key factor affecting electrode impedance. Reducing the electrochemical active area often results in an increase of the impedance of the electrode.[22,38] To demonstrate whether the remarkable impedance change of porous electrodes was derived from the remarkable reduction in the electrochemical active area by binding to the target, the changes in the electrochemical active area and impedance of porous and planar electrodes were measured before and after identification of SARS-CoV-2 RNA (Figure 1F). We first characterized the electrochemical active area of planar and porous electrodes before and after target recognition using cyclic voltammetry (Figures S4 and S5). The electrochemically active surface area of the porous electrode decreased 54-fold after adding SARS-CoV-2 RNA, while the area of the planar electrode decreased only 3.3-fold, indicating that the reduction in the electrochemical active area of the porous electrode is much greater than that of the planar electrode after target binding (Figure 1G). To investigate whether a greater change in electrochemical active area leads to a more remarkable change in impedance, the impedance spectra of planar and porous electrodes modified with probe ss-DNA before and after target recognition were investigated. The impedance signal of the porous electrode was considerably amplified compared with that of the planar electrode (Figure 1H). This result indicates that the porous electrode could induce a more evident change in impedance than the planar electrode did. The above results demonstrate that the substantial impedance change of porous electrodes is due to a greater reduction in electrochemical active area upon binding to the target.

To investigate whether the ss-DNA could hybridize to the target on a porous electrode, we first characterized the spectral changes upon RNA binding using Fourier-transform reflectometric interference spectroscopy (FT-RIFS) (Figure 2A). After being irradiated by incident light, the reflected light at the surface of the porous electrode and the background silicon interface interferes to produce an interference spectrum. Then FT-RIFS can be obtained by appropriate analysis of the Fourier transform of the spectrum. The change in effective optical thickness of the porous layer (2 nL) can be observed intuitively in the FT-RIFS, where n is the refractive index of the porous layer and L is the thickness of the porous layer.[39,40] Increasing the thickness of nucleic acid layer in the pore channels results in a decrease in the refractive index of the porous layer, leading to a blue shift in the 2 nL value.[41] Thus, the 2 nL value can be used to determine the thickness of the nucleic acid layer on the electrode surface. As shown in Figure 2B, a blue-shift in 2 nL occurred when the ss-DNA was
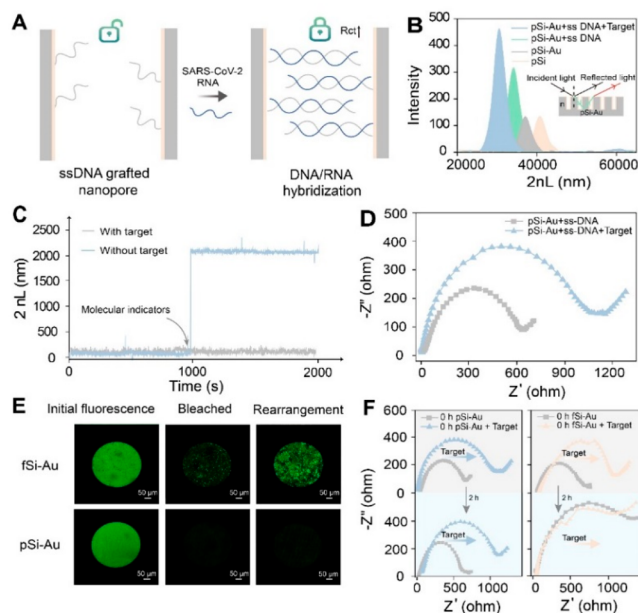

Figure 2. Increased sensitivity and stability of porous electrode by DNA nanolock. (A) Schematic of the changes in impedance of the DNA nanolock porous electrode through the open−closed switching. (B) FT-RIFS of porous silicon (orange), gold-plated porous silicon (gray), gold-plated porous silicon modified with ssDNA (blue), and the counterpart subsequently incubated with target to form double-stranded oligonucleotides in the pore channels (green). The inset shows the basic principles of FT-RIFS. (C) Real-time FT-RIFS of small molecule indicators entering the pore before the porous electrode was closed (without target) and after the porous electrode was closed (with target). The small molecule indicators were added at 1000 s. (D) The impedance spectra of the DNA nanolock porous electrode between open and closed states. The inset shows the simulated circuit diagram. (E) Confocal fluorescence images of the FAM-modified recognition probes on flat and porous electrodes in three successive stages: (i) fluorescence imaging before photobleaching; (ii) fluorescence imaging after photobleaching; and (iii) fluorescence imaging of FAM-modified recognition probes following rearrangement for 2 h. (F) Impedance spectra before and after target recognition on porous electrode (left) and planar electrode (right) at 0 and 2 h; recognition probe concentration: 100 nM.

introduced, confirming that the ss-DNA was successfully modified on a gold-coated porous electrode. When the ss-DNA-modified porous electrode was exposed to solution of SARS-CoV-2 RNA, the 2 nL value of the porous layer revealed a further blue-shift, indicating the increase in the thickness of the nucleic acid layer. According to previous reports,[20] this is due to the ss-DNA complementarily binding to the target RNA to form a more stretched and rigid double-stranded structure, eventually leading to an increase in the thickness of the nucleic acid layer and a decrease in the refractive index.

The adsorption of small molecule indicators on nanopores will affect the optical thickness of the nanopore, thus allowing the changes in permeability of the nanopore to be reflected by the small molecule indicator-induced 2 nL value change.[42,43] To investigate whether the double-stranded nucleic acids block the nanopore, we incubated the small molecule indicators insulin with ss-DNA-modified porous electrodes and used the real-time FT-RIFS to characterize the changes in the 2 nL value before and after ss-DNA binding to target SARS-CoV-2

RNA. It was observed that adding the small molecule indicators into ss-DNA-modified porous electrodes significantly increased the shift in the $2nL$ value (Figure 2C), indicating that small molecule indicators can penetrate into the ss-DNA-anchored channel and be adsorbed to the pore wall in the absence of target RNA. Conversely, when the small molecule indicators of the same concentration were added after ssDNA hybridized with complementary SARS-CoV-2 RNA, the $2nL$ value hardly changed over time (Figure 2C), demonstrating that the small molecule indicators did not enter the nanopore. To determine whether the double-stranded structure closing the nanopore is pivotal in impedance changes, the impedance spectrum characterizations of both single-stranded and double-stranded nucleic acid-modified porous electrodes were performed. The experimental results suggest that the half-circle diameter in impedance of the double-stranded nucleic acid-modified porous electrodes was significantly higher than that of the electrodes modified with single strand, indicating that the formation of double-stranded nucleic acids significantly increased the electrode impedance. This finding is consistent with the results of real-time FT-RIFS (Figure 2D). In summary, the rigid double-stranded nucleic acids cause substantial impedance amplification by closing the nanopores, and this structural change leading to impedance variation is commonly referred to as DNA nanolock.[20]

Improvement of Sensitivity and Selectivity by DNA Nanolock. The thiol-modified recognition probes on the electrode surface can undergo desorption and rearrangement, thereby affecting the stability of the DNA nanolock.[44,45] To investigate the stability of the DNA nanolock on the porous electrode, we first studied the desorption-rearrangement process of the recognition probes on the gold-coated porous electrode surface. The recognition probes were labeled with 6-carboxy-fluorescine (FAM) fluorescent dye and modified on porous and flat electrodes, respectively. The fluorescence intensity of the recognition probes on the two electrodes was monitored in real-time by confocal microscopy (Figure 2E). Before photobleaching, a bright green fluorescence was observed on both electrodes. After continuous irradiation for 10 min, the fluorescence was quenched on the two electrodes. With incubation for 2 h, the fluorescence of the porous electrodes did not recover, while the flat electrodes showed obvious fluorescence recovery. This result suggests that the unbleached DNA probes on the flat electrodes can readily dissociate and reassociate with the bleached regions, while the DNA probes on the porous electrodes remain stable. We also tested the impedance spectra of the recognition-probe-modified porous and flat electrodes to characterize the desorption-rearrangement process. The porous electrodes did not undergo impedance drift after standing for 2 h, and a remarkable impedance response was observed at both 0 and 2 h after recognizing the SARS-CoV-2 RNA (Figure 2F, left panel). By contrast, after 2 h of incubation, the planar electrodes had high levels of background impedance, resulting in an irrational impedance decrease after addition of SARS-CoV-2 RNA at 2 h (Figure 2F, right panel). These data demonstrate that the inhibition of the desorption-rearrangement process was achieved on the porous electrode surface. The stability of the recognition probes on the porous electrode surface can be ascribed to the spatial confinement effect in porous electrodes. When the size of the DNA is similar to that of the nanopore, the rearrangement of DNA at the interface is inhibited, leading to the stabilization of the electrochemical

active area and impedance signal. However, when the pore size is much larger than the size of the DNA, or when the DNA is on a flat electrode, the spatial confinement effect is remarkably weakened. To further demonstrate the influence of the spatial confinement effect on detection reproducibility, we repeated the detection 6 times using the probe-modified porous electrodes with pore size of 40 and 10 nm and the probe-modified flat electrodes and calculated the average error rate. Our results showed that the relative error for the flat electrodes and the porous electrodes with pore sizes of 40 nm were 26% and 16%, respectively, significantly higher than the relative error of 2% for the porous electrodes with pore sizes of 10 nm (Figure S6). The flat electrodes had the largest relative error, indicating that the detection reproducibility can be significantly improved by the spatial confinement effect. The high mobility of thiolated DNA chemisorbed on the planar gold electrode surface has been demonstrated by previous studies.[46,47] The steric-hindrance effect of the nanopore electrode was reported to effectively inhibit the mobility of thiolated DNA molecules across the metal surface and the dissociation of DNA on the electrode. The enhanced stability of the DNA probe on the porous electrode interface herein is consistent with previous findings. Taken together, our results indicate that the spatial confinement effect is critical for maintaining the stability of DNA nanolock and is a requisite for the excellent stability in impedance tests.

Next, the capability of porous electrode sensors to detect SARS-CoV-2 nucleic acid has been investigated. To determine whether the individuals were previously infected with SARS-CoV-2, the SARS-CoV-2 RNA or the cDNA reverse-transcribed from SARS-CoV-2 viral RNA was detected in practice.[4,48] The electrochemical cell for electrochemical etching and electrochemical impedance spectroscopy (EIS) measurements was designed, and the capability of the porous electrode sensors to detect both the SARS-CoV-2 RNA and SARS-CoV-2 cDNA was investigated (Figure 3A). First, the probes targeting the SARS-CoV-2 RNA or the cDNA are functionalized on porous electrodes, respectively. Then, impedance changes are measured upon successive addition of SARS-CoV-2 RNA or cDNA with concentrations ranging from the pM to fM regime. The impedance response of the porous electrode is measured upon successive addition of SARS-CoV-2 RNA or cDNA with concentrations from fM to pM (Figure 3B,C). The results showed that more added targets binding to the pore surface lead to the larger impedance change. The statistical results showed that the $\Delta R_{ct}/R_{ct}$ value of the porous electrode follows a linear relationship with the SARS-CoV-2 RNA or the cDNA concentration on a logarithmic scale, indicating that the nucleic-acid-induced pore blockade is in a target concentration-dependent manner. This linearity could be used for quantitative SARS-CoV-2 nucleic acid testing in actual samples (Figure 3D). Notably, because the cDNA was acquired by reverse transcription, the prolonged cDNA strand and error-prone cDNA synthesis resulted in a lower efficiency in hybridization between cDNA and the capture probe.[49] As shown in Figure S7, the melting-temperature (T_m) of RNA and probe DNA hybrids (68.9 °C) was higher than that of cDNA and probe DNA hybrids (66.4 °C), respectively, demonstrating that the hybrids of RNA and probe DNA were more stable than those of cDNA and probe DNA hybrids. Hence, the slope of the standard curve for cDNA detection was lower than that for RNA detection. The LOD for both SARS-CoV-2 RNA and cDNA was estimated to be as low as about 0.03 fM. The results
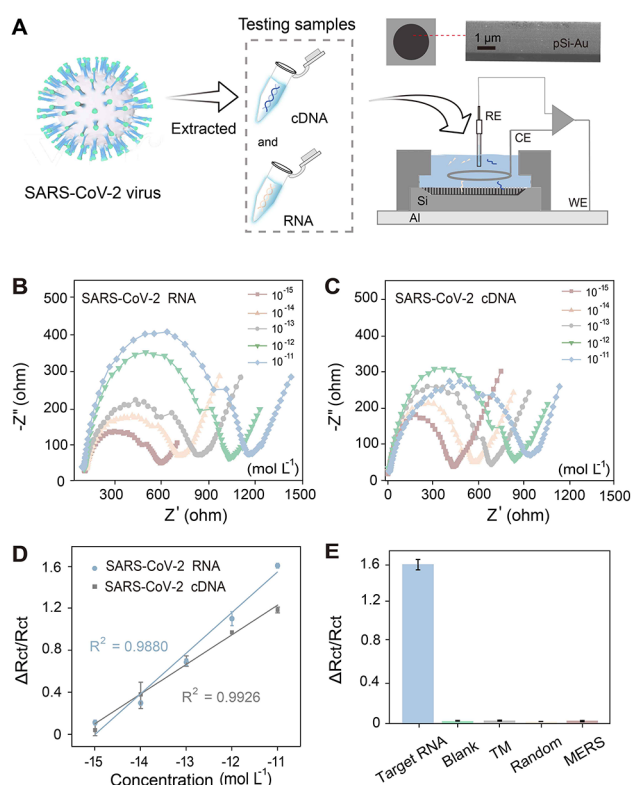
Figure 3. Assessment of the performance of porous electrode on SARS-CoV-2 nucleic acids testing. (A) Schematic diagram of a porous electrode device and the work flow of SARS-CoV-2 nucleic acid testing. The inset shows a photograph and SEM cross-sectional image of the porous electrode. RE: reference electrode; CE: counter electrode; WE: working electrode. Impedance spectra response upon addition of SARS-CoV-2 RNA (B) and cDNA (C) solutions with different concentration (10^{-11} to 10^{-15} M) in buffer solution using the porous electrode sensor. (D) Plots of $|\Delta R_{ct}/R_{ct}|$ of the porous electrode sensor versus SARS-CoV-2 RNA or cDNA concentration. Impedance changes were calculated using the following equations: $\Delta R_{ct}/R_{ct} = (R_{ctf} - R_{ct})/R_{ct}$, where R_{ctf} is the final charge transfer resistance after target sequence addition and R_{ct} is the initial charge transfer resistance measured before addition of target sequence. (E) $|\Delta R_{ct}/R_{ct}|$ response of pSi-Au upon addition of SARS-CoV-2 RNA, MERS-CoV virus RNA, two-base mismatch RNA (TM), and random sequence RNA (Random).

suggested that the porous electrode sensor had a low LOD for SARS-CoV-2 nucleic acids (Table S2) and showed a good linear correlation with the target concentration, indicating that the porous electrode sensor can be used for the high-sensitivity detection of SARS-CoV-2 nucleic acid.

Since the SARS-CoV-2 RNA could be detected after lysis, the direct detection of RNA using a portable device can provide a faster diagnosis of SARS-CoV-2 infection.[50] Therefore, direct analysis of SARS-CoV-2 RNA was performed in the following experiments.[51] Comparing the LOD of porous electrodes for detecting RNA with corresponding measurements of planar electrodes, the results showed that the LOD of the porous electrodes for quantitating SARS-CoV-2 nucleic acid was much lower than that of the planar electrodes (Figures 3D, S8, and S9). This verifies that the nanolock structures in the porous electrodes can cause a greater change in the impedance (Figures 1 and 2). To validate the selective recognition of SARS-CoV-2 virus by the porous electrode sensors, MERS-CoV virus RNA and double-base mismatched

RNA that have molecular structures similar to SARS-CoV-2 RNA and random sequence RNA were selected as the targets for the selectivity experiments. The results showed that SARS-CoV-2 RNA caused a remarkable increase in the diameter of the semicircle of the impedance spectrum, while MERS-CoV virus RNA, double-base mismatched RNA, and random sequence RNA resulted in almost no change in the diameter of the semicircle (Figure S10). This indicates that the impedance change induced by SARS-CoV-2 RNA is much higher than that caused by other targets, showing high specificity in the SARS-CoV-2 nucleic acid testing (Figure 3E). Altogether, these experiments show that this porous electrode sensor has the advantages of ease of use, low detection limit, and good specificity to achieve the detection of SARS-CoV-2 nucleic acids.

Developing a Porous Electrode-Based Portable Device to Detect SARS-CoV-2 RNA in Actual Saliva Samples. To enable portable detection of SARS-CoV-2 RNA, an electrochemical portable device integrating the porous electrode, potentiostat, analog-to-digital converter, and Bluetooth module was designed (Figures S11 and S12 and Table S3). The impedance signals were acquired through the porous electrode and wirelessly transmitted to an accompanying smartphone app (Figure 4A). Since saliva samples are easy to collect and facilitate rapid detection, saliva samples were used for subsequent testing. To investigate whether the porous electrode portable device could detect SARS-CoV-2 RNA in actual saliva samples, different concentrations of SARS-CoV-2 RNA were spiked in actual saliva samples to obtain pseudovirus samples, and the impedance changes in the saliva samples were detected directly by the porous electrode portable device (Figure 4A). As the concentration of SARS-CoV-2 RNA in the sample is increased, the diameter of the semicircular region in the impedance spectrum gradually increases (Figure S13), and the $\Delta R_{ct}/R_{ct}$ value showed a linear dependence upon the SARS-CoV-2 RNA concentration on a logarithmic scale (Figure 4B), indicating that SARS-CoV-2 nucleic acid from actual samples could be detected quantitatively by the portable device. The LOD for pseudovirus obtained from the linear standard curve was about 1 fM. The above results demonstrate that the porous electrode portable device offers accurate and sensitive detection of SARS-CoV-2 nucleic acids in actual saliva samples. The ability of the device to distinguish COVID-19-positive cases among pseudovirus samples was further evaluated. The threshold value was set as 0.37 to distinguish the COVID-19 positive and negative samples (Figure S14). MERS-CoV RNA, PBS buffer, and SARS-CoV-2 RNA were added to the interference group (samples 1−15), control group (samples 16−30), and positive group (samples 31−45), correspondingly. Double-blind testing of pseudovirus samples was performed, and the porous electrode-based portable device was used to distinguish COVID-19-positive cases. The experimental results showed that the signal values of samples 1−10 and 12−30 were lower than the threshold and were considered negative, while the signal values of samples 11 and 31−45 were higher than the threshold and were considered positive (Figure 4C). The accuracy in identifying positive and negative samples was 98%, and the sample exhibited high consistency with gold-standard RT-qPCR results (Table S4 and Table S5). In addition, the box plot showed that the median value of the positive group was 23 and 29 times higher than those of the control and interference groups, respectively
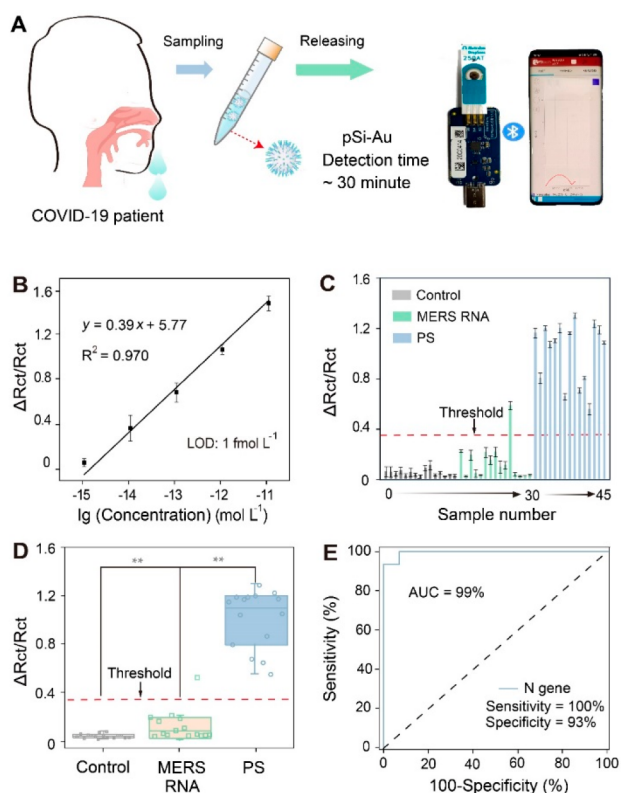
Figure 4. SARS-CoV-2 nucleic acids detection in saliva samples using porous electrode-based portable devices. (A) Schematic of SARS-CoV-2 nucleic acid testing using porous electrode-based portable devices. (B) Calibration curves obtained from the device in (A) in diluted saliva, detecting $|\Delta R_{ct}/R_{ct}|$ values for various concentrations of SARS-CoV-2 RNA in logarithm scale. The error bars represent the standard deviations ($n = 3$). The limit of detection (LOD) is 1 fM. (C, D) $|\Delta R_{ct}/R_{ct}|$ responses (C) and box plot (D) of the detection results upon the addition of MERS virus nucleic acid, blank buffer, and SARS-CoV-2 nucleic acid in full artificial saliva. The threshold is 0.37. Threshold line (red) is plotted as mean readout value for controls plus 3 standard deviations. PS: positive samples. (E) ROC curves generated from the sample data of the porous electrode-based portable device ($n = 45$). The area under the curve (AUC) was 0.99. By applying a threshold (the red dotted line as indicated in panels C and D), this device showed sensitivity of 100% and specificity of 93%.

(Figure 4D). The minimum value of the positive group was much higher than the maximum value of the control and interference groups, indicating that the porous electrode-based portable device could accurately distinguish COVID-19-positive samples from COVID-19-negative samples.

To evaluate the clinical potential of the porous electrode based portable device for detecting SARS-CoV-2 nucleic acids, the receiver operating characteristic (ROC) analysis was conducted to assess the sensitivity and specificity of the device.[52] Based on the testing of 45 pseudovirus samples mentioned above, the threshold was performed using the SPSS Statistical software, and we obtained the ROC curve of the sample data. As shown in Figure 4E, the blue line represents the ROC curve, and the area under the ROC curve (AUC) is 99%, demonstrating that the porous electrode-based portable device had good accuracy toward SARS-CoV-2 nucleic acids. A sensitivity of 100% and a specificity of 93% were achieved based on the optimal detection threshold, and these values are significantly higher than that estimated by electrochemical detection (sensitivity of 92.3% and specificity of 87.5%) and fluorescence detection (sensitivity of 87.0% and specificity of 92.0%).[53,54] These results indicate that the porous electrode-based portable device could enable accurate COVID-19 diagnosis.

CONCLUSION

In summary, this work demonstrates a porous electrode constructed by a DNA nanolock for sensitive and accurate detection of viral nucleic acid. Furthermore, a portable porous electrode-based device is developed for the point-of-care detection of SARS-CoV-2 nucleic acids in saliva samples. After recognizing SARS-CoV-2 nucleic acids, the surface-attached DNA nanolock effectively blocks the pore and therefore reduces the active area of the electrode, resulting in impedance amplification of the porous electrode and great improvement of sensitivity to detect SARS-CoV-2 nucleic acid. Meanwhile, the stability of the DNA nanolock structure can be enhanced by a spatial confinement effect. For the detection of analytes in solution, the impedance change of the porous electrode follows a linear relationship with the SARS-CoV-2 RNA or the cDNA concentration on a logarithmic scale, and the detection limit was estimated as low as 0.03 fM for both SARS-CoV-2 RNA and cDNA. This electrode was also able to reliably distinguish other structurally similar nucleic acids. Additionally, the porous electrode was integrated with a circuit control module to fabricate a portable detection device that can transmit data wirelessly. The device showed high performance in distinguishing SARS-CoV-2 positive cases among 45 double-blind samples with an accuracy of 98%. Under the optimal detection threshold, the porous electrode-based portable device allows for the detection of SARS-CoV-2 RNA with 100% sensitivity and 93% specificity. This portable device has substantial advantages, including quick diagnoses, high sensitivity, good accuracy, and portability, offering an affordable and accessible solution for the point-of-care detection of SARS-CoV-2 viruses. By changing the recognition nucleic acid probes, this device holds promise for the analysis of other infectious viruses in the future and could be potentially translated into standard clinical practice for infectious or critical disease diagnostics and prognosis.

ASSOCIATED CONTENT

ⓢ Supporting Information

The Supporting Information is available free of charge at https://pubs.acs.org/doi/10.1021/acs.analchem.3c03168.

     Reagents and materials, sample characterization, experimental section and supplementary figures (PDF)

AUTHOR INFORMATION

Corresponding Authors

Quan Yuan − *Molecular Science and Biomedicine Laboratory (MBL), State Key Laboratory of Chemo/Biosensing and Chemometrics, College of Chemistry and Chemical Engineering, Hunan University, Changsha 410082, China;* ⓞ orcid.org/0000-0002-3085-431X; Email: yuanquan@whu.edu.cn

Jie Tan − *Molecular Science and Biomedicine Laboratory (MBL), State Key Laboratory of Chemo/Biosensing and Chemometrics, College of Chemistry and Chemical Engineering, Hunan University, Changsha 410082, China;*

⊙ orcid.org/0000-0002-0909-2904; Email: tanjie0416@hnu.edu.cn

Weihong Tan − *Molecular Science and Biomedicine Laboratory (MBL), State Key Laboratory of Chemo/Biosensing and Chemometrics, College of Chemistry and Chemical Engineering, Hunan University, Changsha 410082, China; The Cancer Hospital of the University of Chinese Academy of Sciences (Zhejiang Cancer Hospital), Hangzhou Institute of Medicine (HIM), Chinese Academy of Sciences, Hangzhou 310022, China;* ⊙ orcid.org/0000-0002-8066-1524; Email: tan@hnu.edu.cn

Authors

Zhongnan Huang − *Molecular Science and Biomedicine Laboratory (MBL), State Key Laboratory of Chemo/Biosensing and Chemometrics, College of Chemistry and Chemical Engineering, Hunan University, Changsha 410082, China*

Wenjie Wang − *Molecular Science and Biomedicine Laboratory (MBL), State Key Laboratory of Chemo/Biosensing and Chemometrics, College of Chemistry and Chemical Engineering, Hunan University, Changsha 410082, China*

Yingfei Wang − *Molecular Science and Biomedicine Laboratory (MBL), State Key Laboratory of Chemo/Biosensing and Chemometrics, College of Chemistry and Chemical Engineering, Hunan University, Changsha 410082, China*

Han Wang − *Molecular Science and Biomedicine Laboratory (MBL), State Key Laboratory of Chemo/Biosensing and Chemometrics, College of Chemistry and Chemical Engineering, Hunan University, Changsha 410082, China*

Yimin Pang − *Molecular Science and Biomedicine Laboratory (MBL), State Key Laboratory of Chemo/Biosensing and Chemometrics, College of Chemistry and Chemical Engineering, Hunan University, Changsha 410082, China*

Complete contact information is available at:
https://pubs.acs.org/10.1021/acs.analchem.3c03168

Author Contributions

[#]Z.H. and W.W. contributed equally to this work.

Notes

The authors declare no competing financial interest.

ACKNOWLEDGMENTS

REFERENCES

(1) Kirtane, A. R.; Verma, M.; Karandikar, P.; Furin, J.; Langer, R.; Traverso, G. *Nat. Nanotechnol.* **2021**, *16*, 369−384.
(2) Baker, R. E.; Mahmud, A. S.; Miller, I. F.; Rajeev, M.; Rasambainarivo, F.; Rice, B. L.; Takahashi, S.; Tatem, A. J.; Wagner, C. E.; Wang, L.-F.; et al. *Nat. Rev. Microbiol.* **2022**, *20*, 193−205.
(3) Plante, J. A.; Liu, Y.; Liu, J.; Xia, H.; Johnson, B. A.; Lokugamage, K. G.; Zhang, X.; Muruato, A. E.; Zou, J.; Fontes-Garfias, C. R.; et al. *Nature* **2021**, *592*, 116−121.
(4) Wang, L.; Wang, X.; Wu, Y.; Guo, M.; Gu, C.; Dai, C.; Kong, D.; Wang, Y.; Zhang, C.; Qu, D.; et al. *Nat. Biomed. Eng.* **2022**, *6*, 276−285.
(5) Zhang, T.; Deng, R.; Wang, Y.; Wu, C.; Zhang, K.; Wang, C.; Gong, N.; Ledesma-Amaro, R.; Teng, X.; Yang, C.; et al. *Nat. Biomed. Eng.* **2022**, *6*, 957−967.
(6) Liu, H.; Yang, A.; Song, J.; Wang, N.; Lam, P.; Li, Y.; Law, H. K.-w.; Yan, F. *Sci. Adv.* **2021**, *7*, eabg8387.
(7) Najjar, D.; Rainbow, J.; Sharma Timilsina, S.; Jolly, P.; de Puig, H.; Yafia, M.; Durr, N.; Sallum, H.; Alter, G.; Li, J. Z.; et al. *Nat. Biomed. Eng.* **2022**, *6*, 968−978.
(8) Chaibun, T.; Puenpa, J.; Ngamdee, T.; Boonapatcharoen, N.; Athamanolap, P.; O'Mullane, A. P.; Vongpunsawad, S.; Poovorawan, Y.; Lee, S. Y.; Lertanantawong, B. *Nat. Commun.* **2021**, *12*, 802.
(9) Chandrasekaran, S. S.; Agrawal, S.; Fanton, A.; Jangid, A. R.; Charrez, B.; Escajeda, A. M.; Son, S.; McIntosh, R.; Tran, H.; Bhuiya, A.; et al. *Nat. Biomed. Eng.* **2022**, *6*, 944−956.
(10) Arizti-Sanz, J.; Freije, C. A.; Stanton, A. C.; Petros, B. A.; Boehm, C. K.; Siddiqui, S.; Shaw, B. M.; Adams, G.; Kosoko-Thoroddsen, T.-S. F.; Kemball, M. E.; et al. *Nat. Commun.* **2020**, *11*, 5921.
(11) Arizti-Sanz, J.; Bradley, A. D.; Zhang, Y. B.; Boehm, C. K.; Freije, C. A.; Grunberg, M. E.; Kosoko-Thoroddsen, T.-S. F.; Welch, N. L.; Pillai, P. P.; Mantena, S.; et al. *Nat. Biomed. Eng.* **2022**, *6*, 932−943.
(12) Ghouneimy, A.; Mahfouz, M. *Nat. Biomed. Eng.* **2022**, *6*, 925−927.
(13) Kong, L.; Han, Z.; Zhao, M.; Zhang, X.; Zhuo, Y.; Chai, Y.; Li, Z.; Yuan, R. *Anal. Chem.* **2022**, *94*, 11416−11424.
(14) Zhang, J.; Guo, F.; Zhu, J.; He, Z.; Hao, L.; Weng, L.; Wang, L.; Chao, J. *Anal. Chem.* **2023**, *95*, 11440−11448.
(15) Zhang, J.; Hao, L.; Zhao, Z.; Jiang, D.; Chao, J. *Sens. Actuators, B* **2022**, *369*, 132332.
(16) Ji, D.; Guo, M.; Wu, Y.; Liu, W.; Luo, S.; Wang, X.; Kang, H.; Chen, Y.; Dai, C.; Kong, D.; et al. *J. Am. Chem. Soc.* **2022**, *144*, 13526−13537.
(17) Wang, W.; Foley, K.; Shan, X.; Wang, S.; Eaton, S.; Nagaraj, V. J.; Wiktor, P.; Patel, U.; Tao, N. *Nat. Chem.* **2011**, *3*, 249−255.
(18) Wang, S.; Zhang, J.; Gharbi, O.; Vivier, V.; Gao, M.; Orazem, M. E. *Nat. Rev. Methods Primers* **2021**, *1*, 41.
(19) Slinker, J. D.; Muren, N. B.; Renfrew, S. E.; Barton, J. K. *Nat. Chem.* **2011**, *3*, 228−233.
(20) Feng, J.; Wu, J. *Small* **2012**, *8*, 3786−3790.
(21) Li, F.; Mao, X.; Li, F.; Li, M.; Shen, J.; Ge, Z.; Fan, C.; Zuo, X. *J. Am. Chem. Soc.* **2020**, *142*, 9975−9981.
(22) Liu, G.; Sun, C.; Li, D.; Song, S.; Mao, B.; Fan, C.; Tian, Z. *Adv. Mater.* **2010**, *22*, 2148−2150.
(23) Fan, C.; Plaxco, K. W.; Heeger, A. J. *Proc. Natl. Acad. Sci. U. S. A.* **2003**, *100*, 9134−9137.
(24) An, W.; Gao, B.; Mei, S.; Xiang, B.; Fu, J.; Wang, L.; Zhang, Q.; Chu, P. K.; Huo, K. *Nat. Commun.* **2019**, *10*, 1447.
(25) Devarakonda, S.; Ganapathysubramanian, B.; Shrotriya, P. *ACS Appl. Mater. Interfaces* **2022**, *14*, 150−158.
(26) Takmakov, P.; Vlassiouk, I.; Smirnov, S. *Analyst* **2006**, *131*, 1248−1253.
(27) Gao, P.; Wang, D.; Che, C.; Ma, Q.; Wu, X.; Chen, Y.; Xu, H.; Li, X.; Lin, Y.; Ding, D.; et al. *Nat. Protoc.* **2021**, *16*, 4201−4226.
(28) Ma, Q.; Li, Y.; Wang, R.; Xu, H.; Du, Q.; Gao, P.; Xia, F. *Nat. Commun.* **2021**, *12*, 1573.
(29) Feng, J.; Zhao, W.; Su, B.; Wu, J. *Biosens. Bioelectron.* **2011**, *30*, 21−27.
(30) Tan, J.; Xu, L.; Li, T.; Su, B.; Wu, J. *Angew. Chem., Int. Ed.* **2014**, *53*, 9822−9826.
(31) Lin, V. S.-Y.; Motesharei, K.; Dancil, K.-P. S.; Sailor, M. J.; Ghadiri, M. R. *Science* **1997**, *278*, 840−843.
(32) Zeng, L.; Liu, Y.; Nguyenla, X. H.; Abbott, T. R.; Han, M.; Zhu, Y.; Chemparathy, A.; Lin, X.; Chen, X.; Wang, H.; et al. *Nat. Commun.* **2022**, *13*, 2766.

(33) Dutta Noton, K.; Mazumdar, K.; Gordy James, T. *J. Virol.* **2020**, *94*, No. e00647-20.

(34) Neuman, K. C.; Nagy, A. *Nat. Methods* **2008**, *5*, 491−505.

(35) Xue, C.; Hu, S.; Gao, Z.-H.; Wang, L.; Luo, M.-X.; Yu, X.; Li, B.-F.; Shen, Z.; Wu, Z.-S. *Nat. Commun.* **2021**, *12*, 2928.

(36) Abbondanzieri, E. A.; Greenleaf, W. J.; Shaevitz, J. W.; Landick, R.; Block, S. M. *Nature* **2005**, *438*, 460−465.

(37) Syugaev, A. V.; Zonov, R. G.; Mikheev, K. G.; Maratkanova, A. N.; Mikheev, G. M. *J. Phys. Chem. Solids* **2023**, *181*, 111533.

(38) Cai, D.; Ren, L.; Zhao, H.; Xu, C.; Zhang, L.; Yu, Y.; Wang, H.; Lan, Y.; Roberts, M. F.; Chuang, J. H.; et al. *Nat. Nanotechnol.* **2010**, *5*, 597−601.

(39) Lin, V. S. Y.; Motesharei, K.; Dancil, K.-P. S.; Sailor, M. J.; Ghadiri, M. R. *Science* **1997**, *278*, 840−843.

(40) Pacholski, C.; Yu, C.; Miskelly, G. M.; Godin, D.; Sailor, M. J. *J. Am. Chem. Soc.* **2006**, *128*, 4250−4252.

(41) Feng, J.; Zhao, W.; Su, B.; Wu, J. *Biosens. Bioelectron.* **2011**, *30*, 21−27.

(42) Orosco, M. M.; Pacholski, C.; Sailor, M. J. *Nat. Nanotechnol.* **2009**, *4*, 255−258.

(43) Chhasatia, R.; Sweetman, M. J.; Harding, F. J.; Waibel, M.; Kay, T.; Thomas, H.; Loudovaris, T.; Voelcker, N. H. *Biosens. Bioelectron.* **2017**, *91*, 515−522.

(44) Xu, X.; Makaraviciute, A.; Kumar, S.; Wen, C.; Sjödin, M.; Abdurakhmanov, E.; Danielson, U. H.; Nyholm, L.; Zhang, Z. *Anal. Chem.* **2019**, *91*, 14697−14704.

(45) Vogiazi, V.; de la Cruz, A.; Heineman, W. R.; White, R. J.; Dionysiou, D. D. *Anal. Chem.* **2021**, *93*, 812−819.

(46) Sondag-Huethorst, J. A. M.; Schonenberger, C.; Fokkink, L. G. J. *J. Phys. Chem.* **1994**, *98*, 6826−6834.

(47) Xue, Y.; Li, X.; Li, H.; Zhang, W. *Nat. Commun.* **2014**, *5*, 4348.

(48) Kong, D.; Wang, X.; Gu, C.; Guo, M.; Wang, Y.; Ai, Z.; Zhang, S.; Chen, Y.; Liu, W.; Wu, Y.; et al. *J. Am. Chem. Soc.* **2021**, *143*, 17004−17014.

(49) Shipovskov, S.; Saunders, A. M.; Nielsen, J. S.; Hansen, M. H.; Gothelf, K. V.; Ferapontova, E. E. *Biosens. Bioelectron.* **2012**, *37* (1), 99−106.

(50) Nguyen Hai, T.; Falzarano, D.; Gerdts, V.; Liu, Q. *J. Virol.* **2021**, *95*, No. e00687-21.

(51) de Puig, H.; Lee, R. A.; Najjar, D.; Tan, X.; Soenksen, L. R.; Angenent-Mari, N. M.; Donghia, N. M.; Weckman, N. E.; Ory, A.; Ng, C. F. *Sci. Adv.* **2021**, *7*, eabh2944.

(52) McKinney, S. M.; Sieniek, M.; Godbole, V.; Godwin, J.; Antropova, N.; Ashrafian, H.; Back, T.; Chesus, M.; Corrado, G. S.; Darzi, A.; et al. *Nature* **2020**, *577*, 89−94.

(53) Zhao, H.; Zhang, Y.; Chen, Y.; Ho, N. R. Y.; Sundah, N. R.; Natalia, A.; Liu, Y.; Miow, Q. H.; Wang, Y.; Tambyah, P. A.; et al. *Biosens. Bioelectron.* **2021**, *194*, 113629.

(54) Samacoits, A.; Nimsamer, P.; Mayuramart, O.; Chantaravisoot, N.; Sitthi-amorn, P.; Nakhakes, C.; Luangkamchorn, L.; Tongcham, P.; Zahm, U.; Suphanpayak, S.; et al. *ACS Omega* **2021**, *6*, 2727−2733.